Experimental Verification of Buffet Calculation Procedure using unsteady PSP

Jayanta Panda

Ames Research Center, Moffett Field, California

February 2016

NASA STI Program ... in Profile

Since its founding, NASA has been dedicated to the advancement of aeronautics and space science. The NASA scientific and technical information (STI) program plays a key part in helping NASA maintain this important role.

The NASA STI program operates under the auspices of the Agency Chief Information Officer. It collects, organizes, provides for archiving, and disseminates NASA's STI. The NASA STI program provides access to the NASA Aeronautics and Space Database and its public interface, the NASA Technical Reports Server, thus providing one of the largest collections of aeronautical and space science STI in the world. Results are published in both non-NASA channels and by NASA in the NASA STI Report Series, which includes the following report types:

- TECHNICAL PUBLICATION. Reports of completed research or a major significant phase of research that present the results of NASA Programs and include extensive data or theoretical analysis. Includes compilations of significant scientific and technical data and information deemed to be of continuing reference value. NASA counterpart of peer-reviewed formal professional papers but has less stringent limitations on manuscript length and extent of graphic presentations.

- TECHNICAL MEMORANDUM. Scientific and technical findings that are preliminary or of specialized interest, e.g., quick release reports, working papers, and bibliographies that contain minimal annotation. Does not contain extensive analysis.

- CONTRACTOR REPORT. Scientific and technical findings by NASA-sponsored contractors and grantees.

- CONFERENCE PUBLICATION. Collected papers from scientific and technical conferences, symposia, seminars, or other meetings sponsored or co-sponsored by NASA.

- SPECIAL PUBLICATION. Scientific, technical, or historical information from NASA programs, projects, and missions, often concerned with subjects having substantial public interest.

- TECHNICAL TRANSLATION. English-language translations of foreign scientific and technical material pertinent to NASA's mission.

Specialized services also include organizing and publishing research results, distributing specialized research announcements and feeds, providing information desk and personal search support, and enabling data exchange services.

For more information about the NASA STI program, see the following:

- Access the NASA STI program home page at http://www.sti.nasa.gov

- E-mail your question to help@sti.nasa.gov

- Fax your question to the NASA STI Information Desk at 443-757-5803

- Phone the NASA STI Information Desk at 443-757-5802

- Write to:
  STI Information Desk
  NASA Center for AeroSpace Information
  7115 Standard Drive
  Hanover, MD 21076-1320

NASA/TM—2016–219069
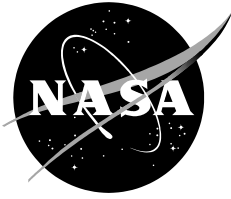
Experimental Verification of Buffet Calculation Procedure using unsteady PSP

Jayanta Panda

Ames Research Center, Moffett Field, California

February 2016

Acknowledgments

The unsteady PSP test was conducted by Ms. Nettie Roozeboom, and Mr. Nate Burnside of NASA Ames, The test was funded by NASA Engineering Safety Center with Dr. David Schuster of NASA Langley and Dr. James C. Ross of NASA Ames as principal investigators.

Experimental Verification of Buffet Calculation Procedure using unsteady PSP

J. Panda

NASA Ames Research Center, Moffett Field, CA 94035

Abstract

Typically a limited number of dynamic pressure sensors are employed to determine the unsteady aerodynamic forces on large, slender aerospace structures. The estimated forces are known to be very sensitive to the number of the dynamic pressure sensors and the details of the integration scheme. This report describes a robust calculation procedure, based on frequency-specific correlation lengths, that is found to produce good estimation of fluctuating forces from a few dynamic pressure sensors. The validation test was conducted on a flat panel, placed on the floor of a wind tunnel, and was subjected to vortex shedding from a rectangular bluff-body. The panel was coated with fast response Pressure Sensitive Paint (PSP), which allowed time-resolved measurements of unsteady pressure fluctuations on a dense grid of spatial points. The first part of the report describes the detail procedure used to analyze the high-speed, PSP camera images. The procedure includes steps to reduce contamination by electronic shot noise, correction for spatial non-uniformities, and lamp brightness variation, and finally conversion of fluctuating light intensity to fluctuating pressure. The latter involved applying calibration constants from a few dynamic pressure sensors placed at selective points on the plate. Excellent comparison in the spectra, coherence and phase, calculated via PSP and dynamic pressure sensors validated the PSP processing steps. The second part of the report describes the buffet validation process, for which the first step was to use pressure histories from all PSP points to determine the "true" force fluctuations. In the next step only a selected number of pixels were chosen as "virtual sensors" and a correlation-length based buffet calculation procedure was applied to determine "modeled" force fluctuations. By progressively decreasing the number of virtual sensors it was observed that the present calculation procedure was able to make a close estimate of the "true" unsteady forces only from four sensors. It is believed that the present work provides the first validation of the buffet calculation procedure which has been used for the development of many space vehicles.

Table I. List of Symbols

P: pressure	c: PSP calibration constant
p: fluctuating part of pressure	ψ: Fourier transform
H : height of cuboid	ϕ: power spectral density
q: dynamic pressure,	f : frequency
U: velocity (ft/s)	Γ : coherence
f : sectional fluctuating force	St : Strouhal frequency
F: zonal fluctuating force	x: axial (streamwise) direction
C_p :fluctuating coefficient of pressure	y: cross-stream direction
Cl : fluctuating lift coefficient	i: sensor index along x
ℓ : calculated correlation length (integral length scale)	j: section index along y

λ: applied correlation length
Δx : Axial separation between sections
L: axial length associated with a buffet zone.
w: width of the buffet zone
A: area of the buffet zone = Lw
n: number of instrumented sections in a buffet zone
I: light intensity measured by a pixel
r: Frame rate, /s
η: total number of frames
t: time
k: index in time, also of camera frame

b: number of pixels used for averaging
σ : standard deviation in shot noise

Superscript/subscript:
*: non-dimensional parameters
†: complex conjugate
rms: root-mean-square
s : sectional force
⁻ : average
ref: reference image, sectional force

I. INTRODUCTION

The fluid-structure interactions leading to significant structural response of aerospace vehicles are broadly categorized into two parts. At lower frequencies (typically below 50 Hz, Kabe et al[1]) unsteady aerodynamic forces can couple to the first few bending and torsional modes of the entire space vehicle or wing surfaces leading to significant, and sometimes catastrophic, responses. The phenomenon is categorized as buffet (NASA SP-8001[2]). At higher frequencies where modal density increases, the surface pressure fluctuations produce vibrational response of the panels, aero-shells and undelaying components (Cockburn & Robertson[3]). This is categorized as vibro-acoustics. The origin of both lies with the pressure fluctuations created by the air flow over the vehicle surface, however for the buffet analysis the pressure fluctuations need to be integrated to determine fluctuations of various component of aerodynamic forces. The motion of the vehicle through the atmosphere produces both steady and unsteady components of forces and moments. The steady component, described via lift, drag, side forces etc., also needs to be determined. The advancement of Computational Fluid Dynamics has replaced some wind tunnel tests to determine the steady part. However, reliable calculations of unsteady forces have remained elusive. Wind tunnel tests of scaled models are required to determine buffet response. An ideal buffet test requires an aeroelastically scaled version of the flight vehicle that is capable of simulating the first few bending vibration modes of the full-scale vehicle. Cole & Hennig[4] performed one such test for 1/10th-scale Atlas-Centaur I vehicle. However such a model carries uncertainties in stiffness, and damping coefficients; besides, the test cost becomes excessive. Many of the current space vehicle development programs use rigid models to measure unsteady forces, [5, 6, 7, 8] which becomes input to the finite element model of the full vehicle to numerically determine the structural response.

Model-scale wind tunnel tests use a reasonable number of unsteady pressure sensors, signals from which are integrated via various schemes to calculate unsteady force.[6, 7, 8, 9, 10] However, even when hundreds of such sensors are deployed the relative coverage over large space vehicles remains sparse. A direct, area-weighted, summation is expected to lead to excessively large net force, therefore various correlation based schemes have been employed to reduce the magnitude.[6, 7, 9, 10] In the buffet community there exists two important questions whose answers the present work seek. First, what is the correct procedure to estimate buffet forces from a limited number of pressure sensors? Second, what is the uncertainty in the calculated forces, and how does the uncertainty reduce with increasing number of sensors? The answer to both questions require direct measurement of the unsteady forces. However, such direct measurement on a flight vehicle is very

difficult. Lee and Tang[11] measured unsteady forces on a wing section in a wind tunnel test using a stiff force balance, yet the applicable frequency range was very small. An attempt by Benoit et al[12] to back calculate forces from deflection measured by accelerometers on a small section of a wing produced large uncertainties. Accelerometers placed on a flight vehicle measure localized response from the sum of all unsteady forces: gust, engine thrust variation, pyro technique etc., in addition to buffet. An attempt to back calculate the forcing function creates confusing outcome[8]. There have been efforts to compare flight measurement from individual pressure sensors with the corresponding ones used in wind tunnel tests[13]; however, the comparison uses pressure fluctuations not force fluctuations. Application of identical procedures to flight and wind tunnel data to calculate force does not validate the calculation procedure, since identical errors are repeated in both calculations. The goal of the present work was to seek the answers to the above questions from a wind tunnel test of a simple model: a flat plate subjected to bluff body shedding. The low-cost, small-scale test was free from various complications of a three-dimensional shape, model vibration etc. The emerging technology of unsteady Pressure Sensitive Paint (PSP) was used to perform high spatial-resolution measurements of surface pressure fluctuations. Data from all of the spatial locations were integrated to find the "true" time history of force fluctuations. Data from selected points (2, 4, 8, 12, and 16, in a parametric study) were used as "virtual" dynamic pressure sensors which were then integrated following a correlation based approach similar to that applied in large wind tunnel tests of aerospace vehicles. A comparison between the "true" and the "modeled" forces ultimately provided answers to the two questions described above.

PSP has become a matured experimental tool to measure *time averaged* surface pressure distribution in model-scale wind tunnel tests.[14, 15] There has been a steady push to increase the frequency sensitivity of the paint and the binder combination to measure unsteady fluctuations. Gregory et al[16] provides a good review of the work. For the present work a PtTFPP-based porous polymer paint manufactured by Innovative Scientific Solutions, Inc. (ISSI) was used to increase frequency response.[17, 18] Adding porosity to the binder creates a microscopically pitted surface onto which the luminescent molecules can be applied. This allows oxygen to reach the luminescent molecules much faster, resulting in a higher frequency response. In addition, the effective surface area of a porous binder is much larger than its non-porous counterpart, resulting in higher radiative intensity. This is counterbalanced by a decrease in the radiative intensity due to increased quenching, since oxygen has much easier access to the luminophore. In previous studies ISSI has shown the frequency response of this paint to be >20 kHz.[17, 18]

At the present time, unsteady PSP is an evolving technology and requires independent validation. A secondary goal of the present report is to examine the noise sources, find suitable data analysis and calibration procedures, and finally to validate the PSP measured data. The first part of the paper (Section III below) is devoted towards that end. The second part of the paper (Section IV) uses the pressure time histories to validate the buffet calculation procedure and to provide answers to the key questions.
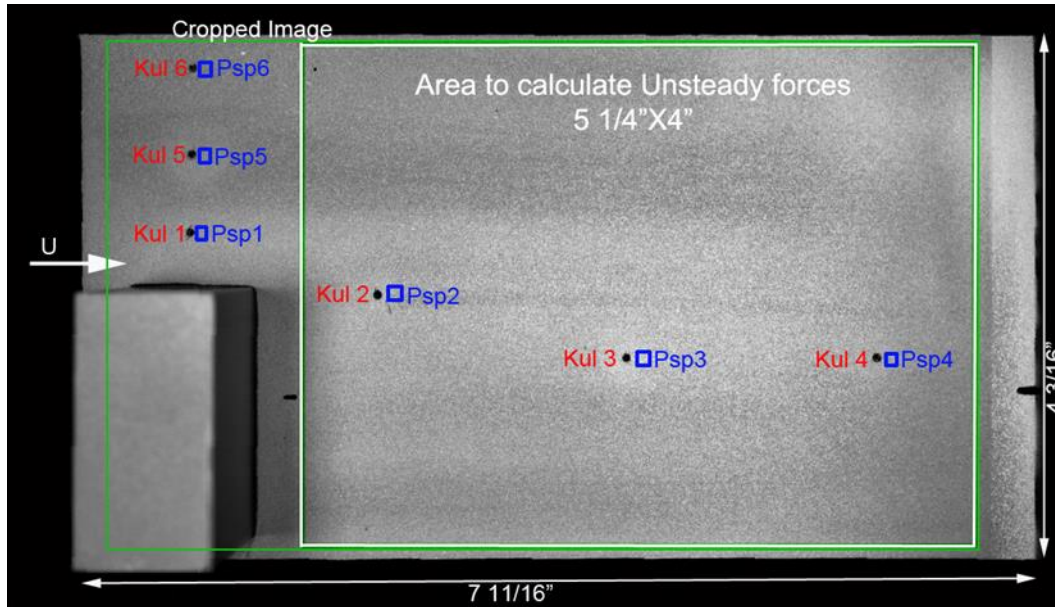
Fig. 1. Photograph of the test article from PSP camera showing 1" (long) X 2" (high) X 2" (wide) cuboid at the leading edge of a PSP painted surface on the wind tunnel floor. The dynamic pressure sensors (Kulites®) are marked as Kul1, Kul2 etc. The corresponding PSP patches used for calibration and comparison are marked as Psp1, Psp2, etc.

II.   EXPERIMENTAL PROCEDURE

The test was conducted in the 14"X14" test section of a small, high-subsonic wind tunnel in the Fluid Mechanics Laboratory of NASA Ames research Center. Various details of the experiment and PSP application procedure can be found in Roozeboom et al[19]; following is a brief description. A part of the wind tunnel floor was replaced by a flush mounted aluminum plate. A solid aluminum block of size 2" (height) x 2" (wide) x 1" (long) was mounted at an off-center position. The pressure fluctuation on the plate was created by flow separation and the periodic vorticity in the wake of the cuboid bluff body. A 7 11/16" (long) x 4 3/16" (wide) part of the plate was coated with PSP (fig 2.). In addition to the pressure sensitive paint, six dynamic pressure sensors were mounted on the plate (one of them, Kul 1, failed). The tunnel was operated at different Mach number conditions; however, data collected only from M= 0.46 (U = 524ft/s) condition will be presented in this paper.

PSP was applied on the plate and also on the aluminum block. For the "Intensity-based" mode of operation, the paint was excited by continuous light at a nominal 396nm wavelength, produced from two high powered ISSI LM4X-DMHP lamps. The luminescence emitted by the PSP was measured with a Phantom v2011 high-speed camera, equipped with a 1200X800 pixel and a 12-bit resolution CMOS chip. To isolate the luminescence frequencies from the incident UV radiation a notch filter in 570nm to 700nm range was placed in front of the camera. A total of 16542 images were recorded at a frame rate of 2000/s. The camera internal memory was capable of holding 16542 frames, the selected frame rate was a compromise between the length of the time record and the frequency range to be resolved. The intensity of light produced by the lamp showed some oscillation just after powering up. Therefore, a delay generator was used to turn the lamps on for a couple of seconds before starting the image acquisition. The light intensity progressively fell over the time of image collection. This drop in the intensity had to be

accounted for. Data from the dynamic pressure transducers (Kulite) was acquired at a higher sampling rate of 30720/s using a 24bit A/D converter in a separate personal computer. No attempt was made to time synchronize the PSP and Kulite data.

III. PSP IMAGE PROCESSING, CALIBRATION AND VALIDATION

The camera images provide time evolution of light intensity distribution over the test article, $I^{//}(x, y, t)$. A comparison of images taken at wind-off and wind-on conditions showed very little movement of the test articles, which precluded the need for image registration. The next step was to examine the noise characteristics and steps to minimize their impact. This is described in section IIIa below. Section IIIb describes corrections due to variation in lamp brightness level, and spatial non-uniformity in paint application. The corrected and normalized intensity distributions were converted to physical pressure fluctuations using calibration constants. The procedure used for calibration was different from that used for traditional steady-state PSP. Since the present interest was only in the fluctuating part of pressure, there was no need to use the traditional absolute pressure vs. absolute intensity calibration from a coupon test. Instead the rms values of the intensity fluctuations were equated with the rms of pressure fluctuations measured by five dynamic pressure sensors. Once an average calibration constant was established the spatio-temporal distribution of pressure fluctuations can be directly established. The frequency and phase responses of the paint are discussed in section IIIc.

IIIa: Noise floor reduction via averaging over increasing number of pixel

An inherent uncertainty in all measurements of light intensity arises due to the random electronic shot noise. Camera images are known to have other noise sources, such as read, thermal, 1/f noise etc. To examine the extent of noise contribution, first, images obtained from the no-flow condition were examined (fig 2). The bottom most plot of fig 2(a) shows time evolution of the count from a single pixel. Since there were no physical pressure fluctuations, the measured fluctuations were artifacts of the camera. The fall in the average intensity with time was due to the falling brightness of the UV lamp described earlier. Figure 2(a) also shows progressively improved smoothening of the time histories caused by averaging over increasing number of pixels. Figure 2(b) provides a quantitative measure via calculation of standard deviation σ of the count fluctuations. Note that the standard deviation was calculated after de-trending the time signal to remove the effect of lamp decay. The standard deviation very closely follows a $b^{-0.5}$ relation, indicating that electronic shot noise is the primary noise source. If the count produced from a single pixel is I, then the standard deviation of shot noise is $\sigma = \sqrt{I}$. If b number of such pixels are averaged then the following relationship holds:

$$\sigma = \frac{\sqrt{b\,I}}{b} \sim \frac{1}{\sqrt{b}}. \qquad (1)$$
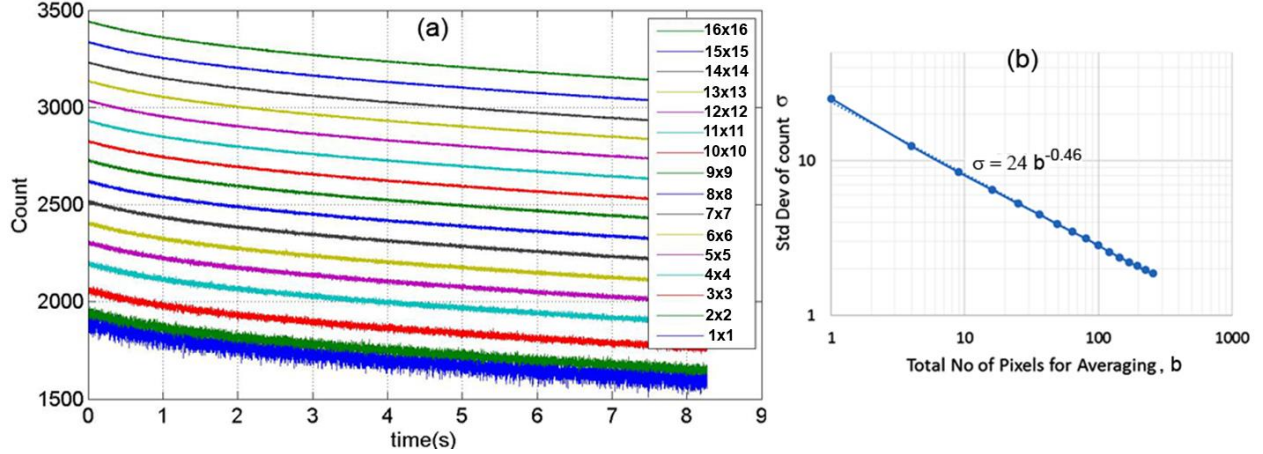
Fig. 2. Reduction in electronic shot noise via averaging over increasing number of pixels, *no-flow, M= 0, images*: (a) Time trace of counts from a single pixel (bottom most, 1x1 in legend) and from averaging over increasing number of indicated pixels. Individual traces are shifted by 100; (b) standard deviation of count fluctuations.
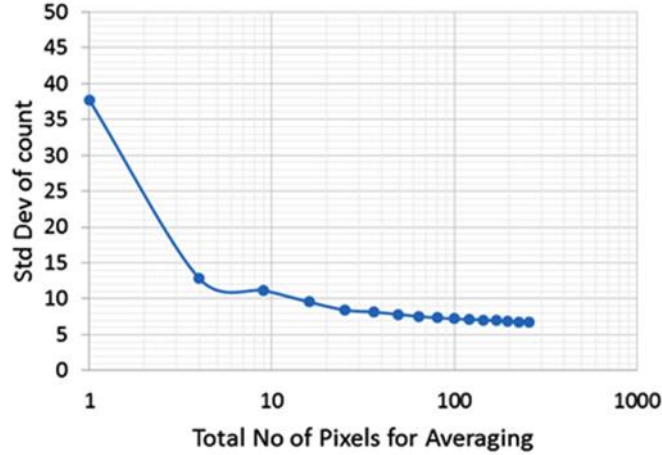
Fig. 3. Same as fig 2(b) above except for M= 0.46 free-stream flow, and a smaller lens aperture.

When the flow was turned on, the test article was subjected to physical fluctuations in pressure, and the shot noise was simply added to the actual fluctuations. Figure 3 shows that the averaging over adjacent pixels makes the standard deviation approach the true value.

The above discussion brings up an important issue of balance between measurement accuracy and the desirable spatial resolution. Addition of the adjacent pixels causes a proportional reduction of spatial resolution Δx. A third factor that comes in play is the frequency-bandwidth Δf that one desires to resolve. An increase in the bandwidth requires a proportional increase in the camera frame rate, i.e., a shorter exposure and fewer photons. For a given set of lamps, camera optics and paint, the radiant flux of photons from the measurement region is fixed. The averaging of the adjacent pixels is equivalent to light collection from a bigger region. A higher frame rate causes a shorter duration for photon accumulation. Therefore the standard deviation of the shot noise is expected to follow the following relationship:

$$\frac{\sigma \Delta x}{\sqrt{\Delta f}} = \text{constant}. \qquad (2)$$

The value of the above constant can be lowered by increasing lamp brightness, using faster optics, using a higher quantum efficiency camera, or by increasing the paint luminescence (by conducting the experiment at higher static pressure). Shot noise ultimately creates a noise floor in the spectra and limits the lowest resolvable amplitude of pressure fluctuations[20]. For the present work, the amplitude of pressure fluctuations were relatively large, and an average over 8x8 (=64) pixels were found to be sufficient to make the noise floor non-identifiable in the power spectra. From this point on, a "pixel" represents the average from 8x8 original pixels.
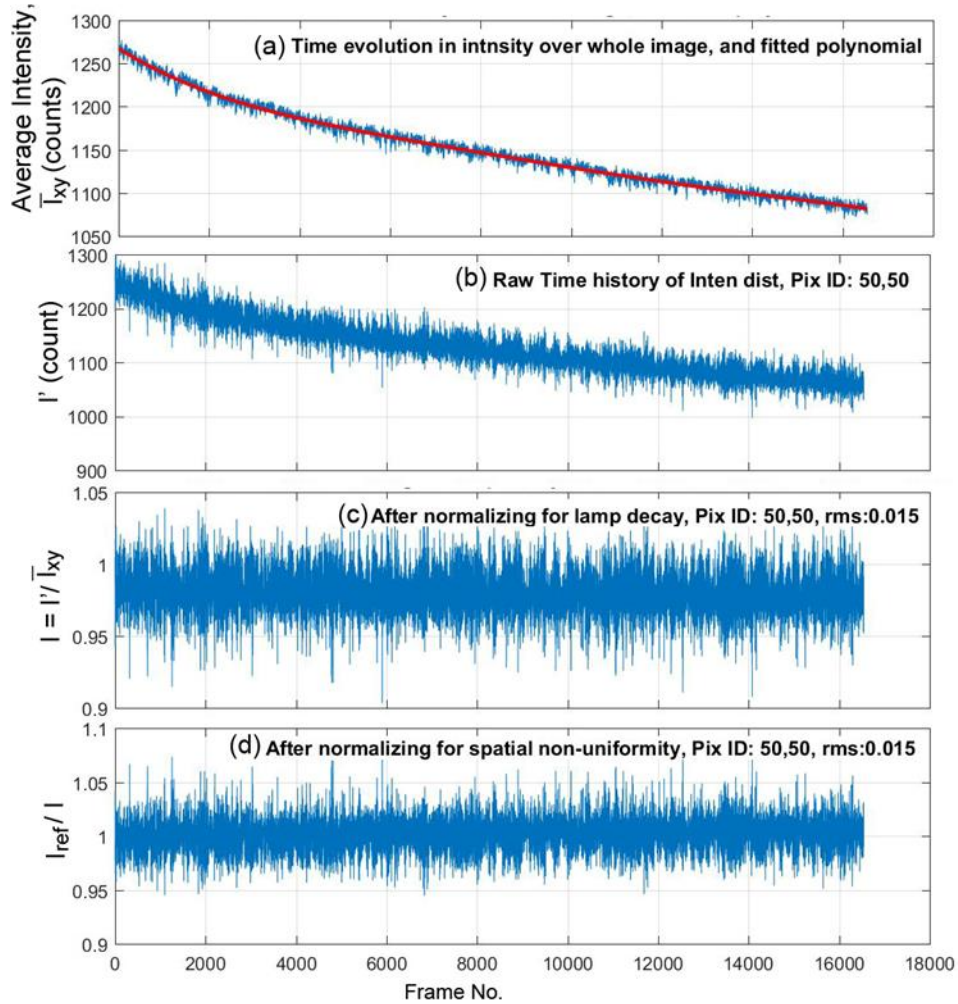
Fig. 4. Steps used to normalize PSP images. (a) Lamp intensity variation measured by averaging all pixels in a frame, and by fitting a polynomial (red line); (b) sample time history of count variation of a single pixel; (c) normalization to account for lamp decay; (d) further normalization by reference image.

IIIb: Corrections and calibration

The first two necessary corrections to the light intensity distribution $I'(x_j, y_i, t_k)$ were to account for the decay in lamp intensity and the spatial non-uniformity of luminescence due to non-uniform paint thickness and other factors. The decay in incident light intensity was established by averaging all pixels over the region of interest for every time frame.

$$\bar{I}_{xy}(t_k) = \frac{1}{no\ of\ pixels} \sum_{i,j} I'(x_j, y_i, t_k) \quad (3)$$

Figure 4(a) shows the time decay of the average intensity. A 7th order polynomial was fitted to the data and the smooth function was then applied to every video frame to adjust for the time-varying illumination:

$$I(x_j, y_i, t_k) = I' / \bar{I}_{xy}. \quad (4)$$

To account for the spatial non-uniformity in the light intensity distribution a reference image was created by averaging all video frames:

$$I_{ref}(x, y) = \frac{1}{\eta} \sum_k I(x_j, y_i, t_k). \quad (5)$$

Subsequently, the reference image was used to normalize each frame I_{ref}/I. Figures 4(b) to 4(d) show the results of the above calculations on a single randomly picked pixel. In the next step, the normalized intensity was converted into engineering units (Pascal) via a calibration process. The intensity of the luminescent light is known to be related to static pressure by the Stern-Volmer formula[14]:

$$\frac{I_{ref}}{I} = A + B \frac{P}{P_{ref}}, \quad (6)$$

Where P is the unknown pressure to be determined via (temperature-dependent) calibration constants A and B, and P_{ref} is a reference pressure. Since I_{ref} represents an average over time instances, $P_{ref} = \bar{P}$, the average static pressure distribution over the plate. Also the large thermal mass of the plate minimized fluctuations in temperature, therefore; A and B were fixed constants. The present interest is in the dynamic, fluctuating part of the pressure which is much smaller than the absolute pressure. Therefore, applying Reynolds decomposition, and also by noting the following:

$$P = \bar{P} + p, \ A + B = 1, \ \frac{I_{ref}}{I} - 1 = \left(\frac{I_{ref}}{I}\right)', \quad (7)$$

the following simple relationship between the fluctuating (normalized) intensity and the fluctuating pressure is reached:

$$p = c\left(\frac{I_{ref}}{I}\right)' \quad where, c = \frac{\bar{P}}{B}. \quad (8)$$

The calibration constant could be easily determined by equating rms fluctuations:

$$p_{rms} = c\left(\frac{I_{ref}}{I}\right)'_{rms}. \quad (9)$$

Specifically, pixel bunches next to each dynamic pressure sensor (Fig. 1) were identified, and the rms of the fluctuations in the frequency interval of $10Hz \leq f \leq 900Hz$ were equated to find the calibration constants (Table II). An average of the calibration constants = 126738Pa was applied to all pixels to determine the space-time distribution of the pressure fluctuations: $p(x_j, y_i, t_k)$. Figure 5 shows one such distribution at one time instance.

Table II. PSP calibration constants from pixels next to the location of a dynamic pressure sensors

Pressure sensor id (Fig 1)	Kul2	Kul3	Kul4	Kul5	Kul6
Calib const c (Pa) =	119016	134274	139355	135590	105452
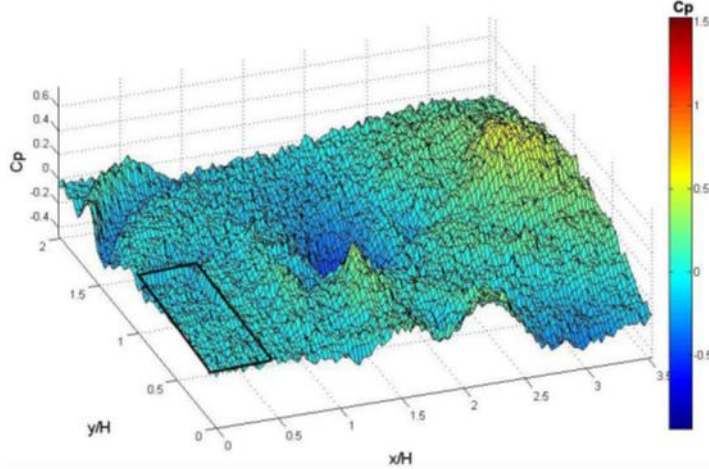
Fig. 5. Distribution of normalized fluctuating pressure on the test plate, at one time instance, measured using PSP.

IIIc: Validation: frequency and phase response of PSP

Power spectra of pressure fluctuations measured by dynamic pressure sensors and by corresponding PSP pixels are compared in fig. 6 (a-e). Good correspondence seen over the entire frequency range, and for all five sensors proves excellent dynamic response of PSP over the frequency range of interest. Flow physics-wise, the hump centered around 420 Hz was due to the periodic vortex shedding by the bluff cuboid, and the very low frequency fluctuations are due to the "breathing" of the separation bubble. Figure 6(f) shows a comparison of the time traces. Note that the PSP camera and the Kulite data acquisition system were not time-synchronized. Therefore, the comparison in fig. 6(f) is only qualitative. Nonetheless, it can be said that the magnitude of PSP time trace is comparable to that from the Kulite sensor, except for the higher frequency content of the latter.

The question of aliasing from the unresolved, higher frequency fluctuations needs to be addressed. The Kulite data were sampled at very high rate with in-built anti-aliasing filter and was free from aliasing. No such anti-aliasing process could be used for the PSP images. For the 2000/s frame rate imaging, the camera shutter was kept opened for nearly the entire 500ns duration of each frame, followed by a fast readout, and a new exposure. This photon accumulation process in effect created an integrate-and-dump filter. Panda & Seasholtz[20] showed that such a process creates a low pass filter with sharp drops around frequencies which are integer multiples of the frame rate. Additionally, an examination of the Kulite data shows continuous decay of spectral energy beyond 1000Hz. Therefore, the effect of aliasing on the PSP data is expected to be small.
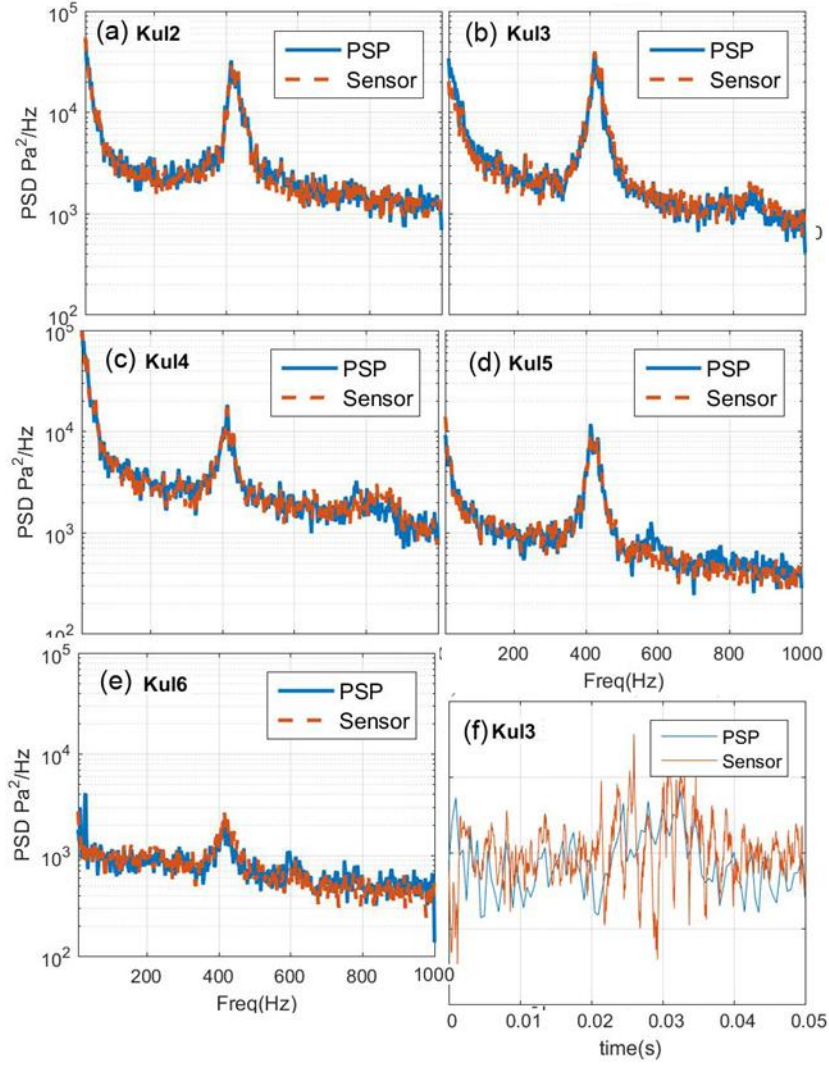
Fig 6. Comparison of (a, b, c, d, e) spectra measured by indicated dynamic pressure transducer and PSP pixel, and (f) time traces of pressure fluctuations
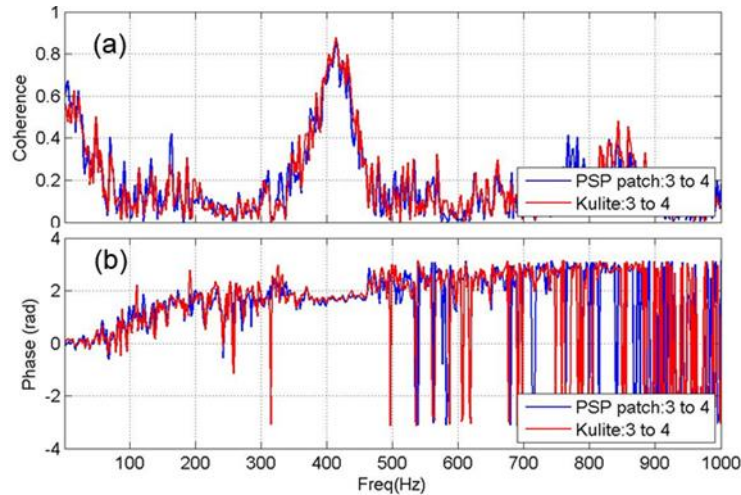
Fig. 7. Comparison of (a) coherence spectra and (b) phase spectra from sensors Kul3 and Kul4, and corresponding PSP pixels: Psp3 and Psp4.

Figure 7 shows the coherence and phase spectra between the two downstream dynamic pressure sensors (see fig. 1.), and the corresponding spectra calculated from PSP pixels adjacent to the sensors. Once again, an excellent comparison proved good phase and amplitude response within the range of interest, below 1 kHz. This paves the path for buffet validation.
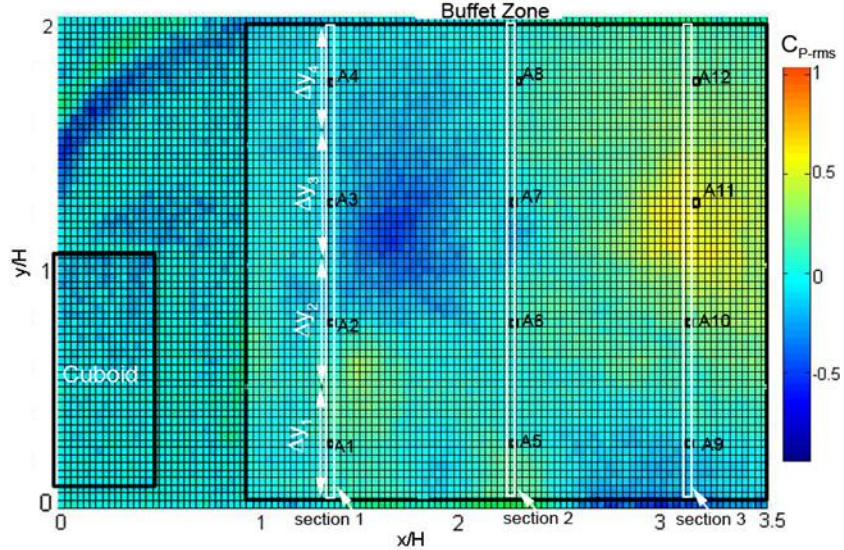
Fig. 8. Distribution of unsteady pressure fluctuations at one time instance, and the selection of the "Buffet Zone" for unsteady force calculations. Each small square represents a pixel that provided time-histories of pressure fluctuations. The "virtual sensors" marked as A1 through A12 were used to calculate the "modeled" force.

IV.   BUFFET FORCE CALCULATION

IVa. Synopsis of the Procedure:

When pressure fluctuations are known over a large number of points, i, j = 1, 2 … N, then the time history of the fluctuating force can be found by a straightforward area weighted summation.

$$F(t) = \sum_{i,j} p_{ij}(x, y, t)\, \delta x_j \delta y_i \qquad (10)$$

The direct summation process does not require the knowledge of correlation among individual measurement points, since the summation naturally accounts for the cancellation due to phase variation, and de-correlation. When the pressure fluctuations are completely uncorrelated, the summation is expected to produce a net zero value. On other hand, if the fluctuations are completely correlated then pressure fluctuations measured from a single sensor provides the unsteady force: F(t) =p(t) A. For most of the real-life applications, pressure fluctuations are only partially correlated over the buffet zone of interest, and an ideal density of sensor distribution should be such that the minimum wavelength of fluctuations of interest should be covered by certain multiples of Nyquist criteria, say 4 sensors. For the present work, the free-stream velocity was U = 524ft/s, and the maximum frequency of interest 1000Hz. Assuming a convection velocity of 0.5U, the minimum wavelength of interest was 3.14 inch. Therefore, sensors placed ~0.78 inch (0.78H) apart should provide a reasonable engineering estimate. The above estimate is for the streamwise direction; in typical boundary layer flows, the convection velocity in the transverse direction is far lower, and may require much denser sensor density. Szechenyi[21] found

that 20 transducers at a single axial station provided reasonable estimate of the sectional, unsteady lift and drag forces on a circular cylinder in cross-flow. Schmidt[22] used 18 such transducers for a similar experiment.

A model-scale wind tunnel test of large aerospace vehicles, typically does not allow for the required sensor density. The entire vehicle (or a component) is divided into "zones", and in each zone lines or rings of relatively closely spaced sensors are mounted; only a few such rings are placed in each buffet zone with relatively long axial separations. The buffet forces are calculated in two steps. First, "sectional force" (i.e. force per unit length, lbf/ft) is estimated from the individual lines/rings. For the present application, transverse lines of "virtual sensors" were initially identified (fig 8) and the sectional forces at every line were calculated,

$$f(j, t) = \sum_i p_{ij}(t)\, \Delta y_i \; . \qquad (11)$$

The sectional forces can be calculated with or without accounting for the lack of correlation along the transverse direction. The method illustrated in this report does not account for the transverse correlation. Notably the original procedure of Dahm[9] and Woods[10], employed during the development of earlier space vehicles, also did not use transverse correlation. In the next step, an average of the sectional forces was estimated:

$$\bar{f}(t) = \sum_{j=1}^{n} f(j,t) \qquad (12)$$

The addition of the time signals in the above equation causes a lowering of rms level, due to cancellation of some of the incoherent fluctuations. Finally, the average sectional force needs to be multiplied by a suitable axial distance to determine the buffet force over a zone. If the sectional forces are completely correlated over the axial length L of the buffet zone, then the net force is simply the following:

$$F_m(t) = L\, \bar{f}(t) \qquad (13)$$

A more general situation is when the fluctuating sectional forces are only partially correlated over the axial distance, such that the integral correlation length is shorter than the length of the buffet zone, $\ell < L$, then the buffet forces are smaller:

$$F_m(t) = \ell\, \bar{f}(t) \qquad (14)$$

There are many different means of determining the correlation length, also called as integral length scale, [6, 7] most of which are oblivious to the multiple flow physics present in a buffet zone, and simply endeavors to determine a single length scale. While certain frequencies of fluctuations, such as those associated with periodic vortex shedding, and oscillation of separated flow can have very long correlation lengths, at other frequencies the length scale can be very short and associated with the random turbulent fluctuations. To account for the variety of flow physics the present paper uses a frequency-specific correlation length approach. In this approach the coherence spectra $\Gamma(j, j+, f_m)$ between the sectional force from a reference section j and that from other available sections j+ were calculated. The decay in coherence with axial separation provided a measure of the integral length scale. The process was repeated for each frequency bin. The underlying assumption in the integral length scale approach is that the pressure fluctuations on the body surface is random (Hinge[23]), such that an exponential function can be used to model the decay in coherence:

$$\Gamma = \exp(-\Delta x / \ell), \quad such\ that \int\limits_0^\infty \Gamma\, dx = \ell \qquad (15)$$

When the fluctuations are periodic, such as due to vortex shedding, then the exponential decay function does not provide a good model (Hinge[23]), however; the estimated length scale becomes very large, and almost always the entire length of the buffet zone (equation 13) is used in the zonal force estimate. This particular ability of differentiating length scale associated with different frequencies makes the present approach a superior choice.

For the following calculation a part of the plate was first selected as the buffet zone (fig. 8). There were a total of 5376 pixels in this zone, providing exceptionally dense distribution of the measurement points. The physical separation between adjacent pixels was 0.064 inch. Recall that the wavelength associated with the highest frequency fluctuation of interest was 3.14 inches. Therefore the shortest eddy was resolved by ~25 measurement points.

IVb. "True" fluctuating force on the buffet zone:

For the actual force calculations following non-dimensional parameters are used:

$$x^* = \frac{x}{H},\ y^* = \frac{y}{H},\ C_P = \frac{p}{q},\ Cl = \frac{F}{0.5\,q\,A},\ Cl_s = \frac{f}{0.5\,q\,w},\ St = \frac{fH}{U} \qquad (16)$$

The dense measurement points allowed for the direct calculation of the unsteady normal force with high level of accuracy. The non-dimensional "true" lift force fluctuations were calculated as following.

$$Cl(t) = \sum_{i,j} C_{p-ij}\, \delta x_j^* \delta y_i^* \qquad (17)$$

The time-series data (fig 9a) was then used to calculate power-spectrum (fig 9b).
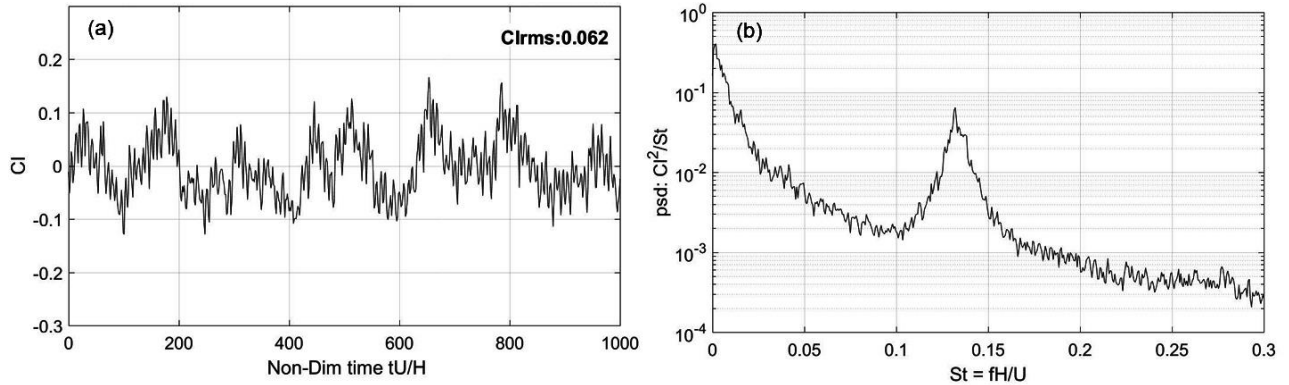
Fig. 9. (a) Time history and (b) power-spectrum of the "true" unsteady lift force on the buffet zone calculated via direct summation of the PSP pixels.

IVc "Modeled" fluctuating force using "virtual sensors":

Out of the 5376 measurement points in the buffet zone, only 12 points, arranged in three axial bunches, were selected for correlation-based estimate (Fig 8). The 12 points effectively represented 12 dynamic pressure transducers placed in the buffet zone. As discussed earlier, the first step was to determine sectional forces for each of the three transverse bunches of virtual sensors after allocating transverse distances Δy_i^* to each:

$$Cl_{s-j}(t) = \sum_i C_{p-i}(t) \Delta y_i^* \, , i = 1, \dots 4; \; j = 1, 2, 3 \quad (18)$$

The time histories of the sectional forces are shown in Fig. 10(a).
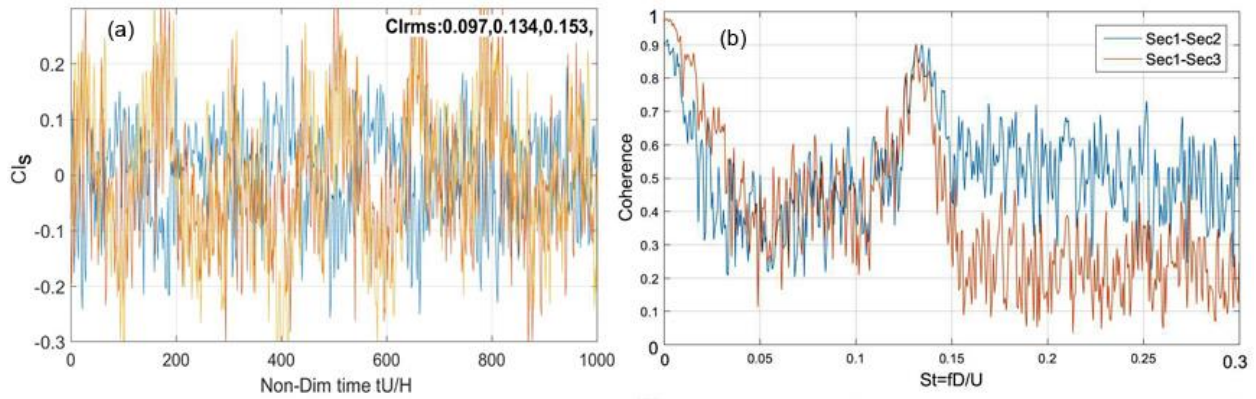
Fig. 10. (a) Time histories of sectional forces calculated from the three columns of virtual sensors, and (b) coherence spectra between indicated sectional forces.
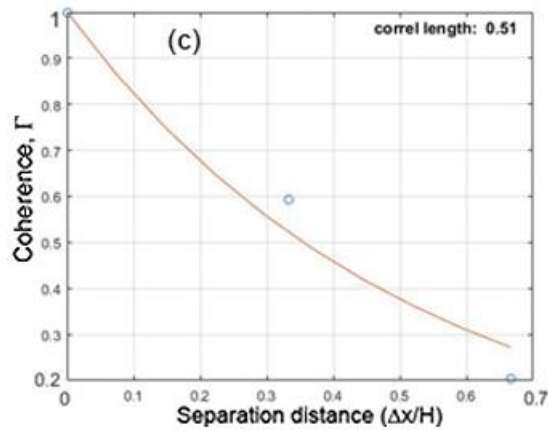
Fig. 11. Calculation of integral (correlation) length via fitting an exponential decay curve to the coherence values at St = 0.18;
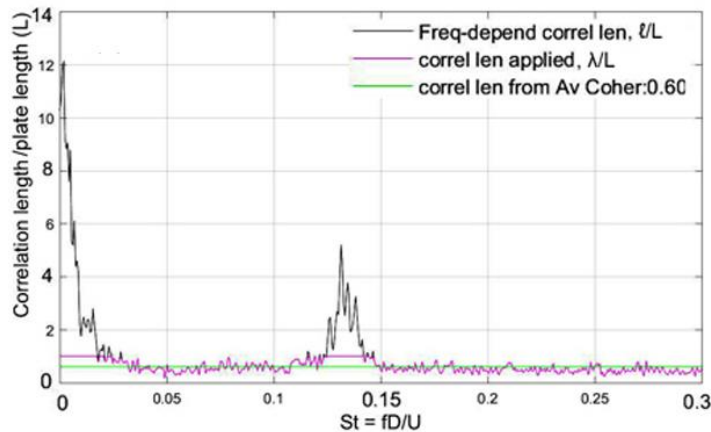
Fig. 12. Spectrum of correlation length calculated (black) and applied (purple). .

The average of the three sectional time forces were then calculated:

14

$$\overline{Cl}_s(t) = \frac{1}{n}\sum_{j=1}^{n=3} Cl_{s-j}(t) \qquad (19)$$

The next step involved determining the spectrum of correlation lengths, for which coherence spectra between the adjacent sectional forces provide an easier path. To improve convergence, the time series $Cl_{s-j}(t_k)$, $k = 1, 2,\ldots \eta$, was segmented into N overlapped sets, each s = 512 long. Discrete Fourier transforms were applied to each set, providing a realization in the statistical ensemble. The realizations from one reference sectional force (represented by the subscript j) and a target sectional force (represented by subscript j+) were used to determine the coherence spectra:

$$\Gamma^2(j, j+, f_m) = \frac{\{\psi(Cl_{s-j})\psi^\dagger(Cl_{s-j+})\}}{\{\psi(Cl_{s-j})\psi^\dagger(Cl_{s-j})\}\{\psi(Cl_{s-j+})\psi^\dagger(Cl_{s-j+})\}} \qquad (20)$$

where, $m = -(s/2-1),\ldots 0,1,\ldots s/2$, and $f_m = mr$.

The curly brackets in the above equation represents expected values or a statistical ensemble over all realizations. Note that the above equation provides magnitude square of coherence. A square root was applied before proceeding to the correlation length calculation. Figure 10(b) shows the coherence spectra calculated using sectional force from station 1 as reference. Note that equation (20) provides a double sided spectrum which is symmetric about the f = 0 band; only the positive frequency parts are shown in fig. 10(b).

Once the coherence spectra were calculated between section1 and section2, and again between section1 and section3, an exponential fit described in equation (15) above was employed to determine the correlation length at every frequency band f_m, $m = -(s/2 -1),\ldots 0,$ $\ldots s/2$. Figure 11 shows an example fit of the exponential function for the St=0.18 band. The abscissa is the streamwise separation distance between the stations where sectional forces were evaluated. The calculated and applied spectra of correlation lengths are shown in fig. 12. The differences between the two occur at frequencies of vortex shedding and the very low frequency "breathing" of the separated flow, which cause the calculated correlation length to become longer than the streamwise extent L of the buffet zone. For such instances, as described in equation (13), the applied length was set to L. A symbolic representation is the following:

$$\lambda(f_m) = \ell(f_m), \text{ when } \ell < L; \quad \lambda(f_m) = L, \text{when } \ell \geq L. \qquad (21)$$

Fig. 12 also shows a constant, frequency-independent, correlation length (in green) which was calculated based on the average coherence over the entire frequency range. Such a constant value is in use within the buffet community. For the present example, use of a constant correlation length would have made a non-conservative estimate of buffet forces at the vortex shedding and very low frequencies.

In the next step, the spectrum of correlation length was applied to the average sectional force to determine the total fluctuating force. This is performed in the frequency domain in three steps:

   (a) Fourier transform of the time history of average sectional force.
   (b) Multiplication by the spectrum of correlation length.
   (c) An inverse Fourier transform to return back to the time domain.

Note that unlike the process for calculating coherence spectra, the time series data $\overline{Cl}_s(t_k)$, $k = 1, 2,\ldots \eta$ cannot be segmented for the present step. Therefore, the double sided Fourier transform produced finer frequency bands f_{m*}:

15

$$\left\{\psi\left(\overline{Cl}_s\right)\right\}(f_{m^*}), \quad m^* = (-\eta/2-1),...,0,...\eta/2 \qquad (22)$$

The spectrum of correlation lengths calculated above was them interpolated in these finer bands:

$$\lambda(f_m) \rightarrow \lambda(f_{m^*}) \qquad (23)$$

This allowed multiplication in the frequency domain and subsequent inverse Fourier transform which resulted into the desired time history of the correlation-adjusted buffet force:

$$Cl(t_k) = \psi^{-1}\left\{\lambda\psi\left(\overline{Cl}_s\right)\right\}, \quad k = 1, 2,...\eta \qquad (24)$$
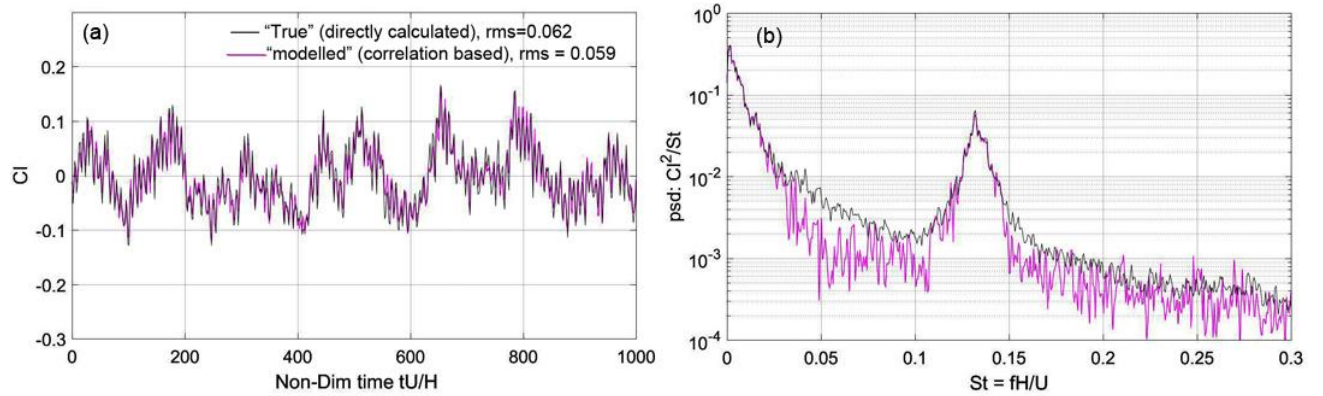
Fig 13. A comparison of "true" and "modeled" (a) time histories, and (b) power spectra of fluctuating lift forces on the buffet zone. The model used 12 "virtual sensors."

The comparison plots between the true and the modeled lift fluctuations in fig. 13 show good similarity that ultimately validates the buffet calculation procedure described above. Recall that only 12 measurement points were used for the "model" calculations while pressure fluctuations at 5376 points were used to determine the "true" fluctuations. The spectral levels of the modeled force are lower than actual in frequency bands where random turbulence dominates. The reason for this difference became apparent in the following parametric study.

IVd. Parametric study: error in buffet calculation from increasing number of "virtual sensors"

The analysis above used 12 virtual sensors arranged in 4(per transverse section) x 3(axial stations). For the parametric study, the number of virtual sensors were changed to 1x2, 2x2, 4x2, 4x3 and 4x4, arranged with equal separation. The time histories of the "modeled forces" were calculated following the procedure described above. Figure 14 shows a comparison of the power spectra; the corresponding rms levels are plotted in fig. 15. An examination of these two figures show reasonable reproduction of the true spectrum for all but the fewest (1x2) case. Particularly, the spectral peaks at the primary flow physics of vortex shedding and low-frequency "breathing" were correctly captured. This proves the robustness of the present calculation scheme. Away from the primary physics, in the frequency bands where pressure fluctuations are less coherent, an increase in the number of sensors was found to progressively decrease the spectral level. An explanation lies with the double accounting for de-correlation for such frequencies, inherent in the procedure. As mentioned earlier, the summation of pressure fluctuations applied to calculate the sectional forces and their average (equations 18 and 19), inherently accounted for the de-correlation in the random fluctuations. Application of the correlation length shorter than the zonal length is equivalent to a repeat deduction which leads to a lowering of the spectral level.

16

This supports the intuitive expectation that the use of large number of dynamic pressure sensor precludes the need for the correlation based approach.
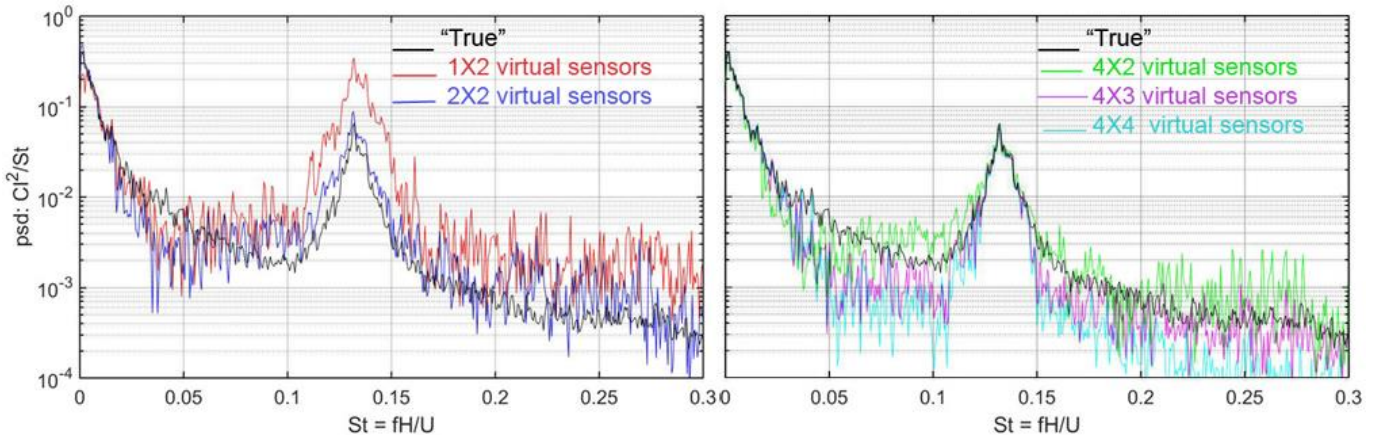
Fig. 14. Comparison between "true" (black) and "modelled" (indicated) power spectra of fluctuating lift forces with increasing number of "virtual sensors".
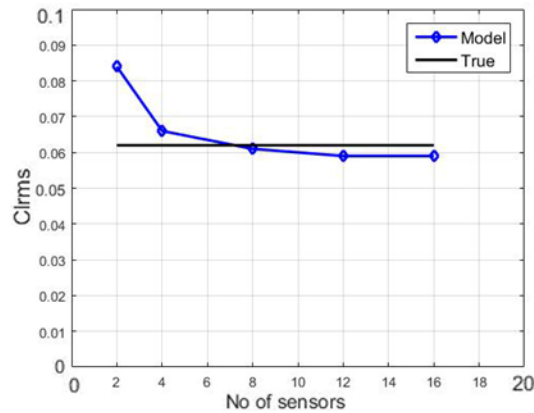
Fig. 15. Effect of increasing "virtual sensors" on the computed rms of force fluctuations.

V. SUMMARY

The present paper attempts to put two measurement technologies on more solid foundations: time-varying pressure fluctuations from unsteady PSP, and estimation of unsteady forces from a sparse number of unsteady pressure sensors. A subsonic wind tunnel test (M= 0.46) of a flush mounted plate, coated with unsteady PSP binder and paint, and subjected to pressure fluctuations from a bluff-body separation provided a simple platform for an in-depth analysis. The paper lays down the detailed and step-by-step procedures for both unsteady PSP analysis and buffet force calculations which also allowed for investigation into the error sources.

Like all other optical techniques that depend on measuring absolute intensities, the PSP images were found to be contaminated by electronic shot noise. Shot noise level was reduced by averaging adjacent pixels, which also led to a reduction of the available spatial resolution. Detailed discussion of these opposing requirements is provided in the text. For the present purpose an average over 8X8 pixels was found to significantly reduce shot noise floor. The PSP images also needed to be corrected for changes in the lamp brightness and spatial non-uniformity from the paint application. In the next step, the light intensity fluctuations were converted to

pressure fluctuations via calibration constants calculated from five unsteady pressure transducers placed on the plate. A simple linear relationship was derived between the normalized fluctuations of luminescence and unsteady pressure fluctuations. Over the relatively modest frequency band of interest: f ≤ 1 kHz, PSP derived power, phase and coherence spectra showed excellent match with the corresponding ones calculated from dynamic pressure sensors. Application of the calibration constant converted the PSP high-speed videos to time histories of pressure fluctuations over an unprecedented number of spatial points that could not be obtained otherwise.

The detailed time histories were used to determine the normal force fluctuations on the plate. While unsteady PSP paves the path for direct measurement of forces in future wind tunnel tests, the existing procedure is to employ a sparse set of dynamic pressure sensors, and to use a correlation length based modeling procedure to achieve that end. The present work employed a frequency-specific, correlation based approach, originally introduced during the Space Shuttle program[7]. The approach assigns longer correlation lengths to coherent sources, such as periodic vortex shedding, flow separation and shock oscillation, and shorter lengths to incoherent random fluctuations. The procedure, like all other currently in use, could not be verified before.

The present small scale test provided an opportunity towards this end. The high-resolution pressure time histories from all 5376 spatial points were at first directly added (with area weight) to establish the "true" force fluctuations. In the next step a parametric study was conducted by selecting only 2, 4, 8, 12 and 16 spatial points ("virtual sensors") to determine the same normal force via the correlation based approach. Except for the fewest 2-point case, the present approach was found to produce reasonable match of both time history and power spectrum of the "true" fluctuations. A closer look revealed that the technique correctly reproduced the levels due to long coherent component for almost all combination of "virtual sensors," yet as their number was increased contribution from the random, weaker fluctuations fell short of the true value. It was pointed out that the first step in the calculation procedure, determining average sectional force, already accounted for the small spatial coherence of the random fluctuations. An application of the shorter correlation length to the sectional forces was equivalent to an unwarranted second deduction. A mere 4 virtual sensors were found to strike the right balance and provided the best reproduction of the true fluctuations for the present case of a flat panel. The best combination for other geometries, such as axisymmetric bodies needs to be established by separate experiments. Nevertheless, the present work represents first comprehensive validation of the buffet force calculation procedure that has been used for the development of many aerospace vehicles.

Reference:
[1]Kabe, A. M. "Design and Verification of Launch and Space Vehicle Structures," AIAA paper 98-1718, 1998.
[2]NASA SP-8001 (1970) Buffeting during atmospheric ascent, NASA Space Vehicle Design Criteria (Structures). May 1964, revised November 1970.
[3]Cockburn, J.A., and Robertson, J.E., "Vibration response of spacecraft shrouds to in-flight fluctuating pressures," J. Sound & Vib., 33(4), pp. 399–425, 1974.
[4]Cole, S. R. & Hennig, T. L. "Dynamic Response of a Hammerhead Launch Vehicle Wind-Tunnel Model," NASA TM-104050, 1991
[5]Jones, G. W., & Foughner, J. T., "Investigation of Buffet Pressures on Models of Large Manned Vehicle Configurations," NASAS TN D-1633, 1963

18

[6]Piatak, D.J., Sekula, M.K., and Rausch, R.D., "Ares Launch Vehicle Transonic Buffet Testing and Analysis Techniques". AIAA Paper No. 2010-4369. Presented at the 28th Applied Aerodynamics Conference, Chicago, IL, 28 June – 1 July, 2010

[7]Panda, J., Martin, F. W., Sutliff, D. L., "Estimation of the Unsteady Aerodynamic load on Space Shuttle External Tank Protuberances from a Component Wind Tunnel Test," AIAA paper 2008-0232, presented at AIAA Aerospace Sciences Meeting, 2008.

[8]Ragab, M, M., "Contribution of Buffet to Space Vehicle Loads during Atmospheric Flight," AIAA paper 92-0716, 1992.

[9]Dahm, W. K. "Composite Model of a Random Forcing Function for the Excitation of a Long Pipes by a Cross Flow," NASA Marshall Space Flight Center Memo no. ED31-79-15, Aug. 1979.

[10]Woods P. (handwritten notes) "Sample Calculations for ET LO2 Feed-line Loads (Generated by Random Vortex Shedding and Aeroacoustic Pressure Fluctuations), Nov. 1979.

[11]Lee, B.H.K. & Tang, F.C., "Transonic Buffet of a Supercritical Airfoil with Trailing-Edge Flap," *J. Aircraft*, **26**(5), pp 459-464, 1989.

[12]Benoit, B. & Legrain, I., "Buffeting Prediction for Transport Aircraft applications Based on Unsteady Pressure Measurements", AIAA paper 87-2356, 1987.

[13]Piatak, D. J., Sekula, M. K., Rausch, R. D. "Comparison of Ares I-X Wind –Tunnel Derived Buffet Environment with Flight Data", AIAA paper 2011-3013, 2011.

[14]Bell, J. H., Schairer, E.T., Hand, L. A. & Mehta, R. D. "Surface pressure Measurements Using Luminescent Coatings," *Ann. Rev. Fluid Mech.* **31**, pp. 155-206, 2001.

[15]Sellers, M.E., "Demonstration of a Temperature Compensated Pressure Sensitive Paint on the Orion Launch abort Vehicle" AIAA paper 2011-3166, 2011.

[16]Gregory, J. W., Sakaue, H., Liu, T, Sullivan, J. P., "Fast Pressure-Sensitive Paint for Flow and Acoustic Diagnostics," *Ann. Rev. Fluid. Mech.*, 2014.

[17]Crafton, J., Forlines, A., Palluconi S., Hsu K., Campbell, C. & Gruber, M., "Investigation of Transverse Jet Injections in a Supersonic Cross flow Using Fast Responding Pressure-Sensitive Paint", AIAA Paper 2011-3522, 2011.

[18]Flaherty, W., Reedy, T.M., Elliot, G.S., Austin, J.M., Schmit, R. F., & Crafton, J. "Investigation of Cavity Flow Using Fast-Response Pressure Sensitive Paint." AIAA Paper 2013-0678, 51st AIAA Aerospace Sciences Meeting, Grapevine, TX, January 2013.

[19]Roozeboom, N.H., Diosady, L.T. , Murman, S.M., Burnside, N. J., Panda ,J., & Ross, J.C. "Unsteady PSP Measurements on a Flat Plate Subject to Vortex Shedding from a Rectangular Prism", AIAA paper 2016-2017, presented at SciTech2016, Jan. 2016.

[20]Panda, J. & Seasholtz, R. G. "Experimental investigation of density fluctuations in high-speed jets and correlation with generated noise," *J. Fluid Mech.*, vol. 450, pp. 97-130, 2002.

[21]Szechenyi, E. "Supercritical Reynolds number simulation for two-dimensional flow over circular cylinders," *J. Fluid Mech.,* **70**(3), pp. 529–542, 1975.

[22]Schmidt, L.V. "Measurement of fluctuating air loads on a circular cylinder," *J. of Aircraft*, **2**(1), pp. 49–55, 1965

[23]Hinge, J, O, *Turbulence,* McGraw-Hill, 1975.